Production of ω mesons in $p + p$, $d +$ Au, Cu $+$ Cu, and Au $+$ Au collisions at $\sqrt{s_{NN}} = 200$ GeV

A. Adare,[11] S. Afanasiev,[27] C. Aidala,[12,41] N. N. Ajitanand,[58] Y. Akiba,[52,53] H. Al-Bataineh,[47] A. Al-Jamel,[47] J. Alexander,[58] A. Angerami,[12] K. Aoki,[34,52] N. Apadula,[59] L. Aphecetche,[60] Y. Aramaki,[10] R. Armendariz,[47] S. H. Aronson,[5] J. Asai,[53] E. T. Atomssa,[35] R. Averbeck,[59] T. C. Awes,[48] B. Azmoun,[5] V. Babintsev,[22] M. Bai,[4] G. Baksay,[18] L. Baksay,[18] A. Baldisseri,[14] K. N. Barish,[6] P. D. Barnes,[37,*] B. Bassalleck,[46] A. T. Basye,[1] S. Bathe,[6,53] S. Batsouli,[12,48] V. Baublis,[51] F. Bauer,[6] C. Baumann,[42] A. Bazilevsky,[5] S. Belikov,[5,26,*] R. Belmont,[64] R. Bennett,[59] A. Berdnikov,[55] Y. Berdnikov,[55] J. H. Bhom,[67] A. A. Bickley,[11] M. T. Bjorndal,[12] D. S. Blau,[33] J. G. Boissevain,[37] J. S. Bok,[67] H. Borel,[14] K. Boyle,[59] M. L. Brooks,[37] D. S. Brown,[47] D. Bucher,[42] H. Buesching,[5] V. Bumazhnov,[22] G. Bunce,[5,53] J. M. Burward-Hoy,[37] S. Butsyk,[37,59] C. M. Camacho,[37] S. Campbell,[59] A. Caringi,[43] J.-S. Chai,[29] B. S. Chang,[67] J.-L. Charvet,[14] C.-H. Chen,[59] S. Chernichenko,[22] C. Y. Chi,[12] J. Chiba,[30] M. Chiu,[5,12,23] I. J. Choi,[67] J. B. Choi,[8] R. K. Choudhury,[3] P. Christiansen,[39] T. Chujo,[63,64] P. Chung,[58] A. Churyn,[22] O. Chvala,[6] V. Cianciolo,[48] Z. Citron,[59] C. R. Cleven,[20] Y. Cobigo,[14] B. A. Cole,[12] M. P. Comets,[49] Z. Conesa del Valle,[35] M. Connors,[59] P. Constantin,[26,37] M. Csanád,[16] T. Csörgő,[31] T. Dahms,[59] S. Dairaku,[34,52] I. Danchev,[64] K. Das,[19] A. Datta,[41] G. David,[5] M. K. Dayananda,[20] M. B. Deaton,[1] K. Dehmelt,[18] H. Delagrange,[60] A. Denisov,[22] D. d'Enterria,[12] A. Deshpande,[53,59] E. J. Desmond,[5] K. V. Dharmawardane,[47] O. Dietzsch,[56] A. Dion,[26,59] M. Donadelli,[56] J. L. Drachenberg,[1] O. Drapier,[35] A. Drees,[59] K. A. Drees,[4] A. K. Dubey,[66] J. M. Durham,[59] A. Durum,[22] D. Dutta,[3] V. Dzhordzhadze,[6,61] L. D'Orazio,[40] S. Edwards,[19] Y. V. Efremenko,[48] J. Egdemir,[59] F. Ellinghaus,[11] W. S. Emam,[6] T. Engelmore,[12] A. Enokizono,[21,36,48] H. En'yo,[52,53] B. Espagnon,[49] S. Esumi,[63] K. O. Eyser,[6] B. Fadem,[43] D. E. Fields,[46,53] M. Finger,[7,27] M. Finger Jr,[7,27] F. Fleuret,[35] S. L. Fokin,[33] B. Forestier,[38] Z. Fraenkel,[66,*] J. E. Frantz,[12,59] A. Franz,[5] A. D. Frawley,[19] K. Fujiwara,[52] Y. Fukao,[34,52] S.-Y. Fung,[6] T. Fusayasu,[45] S. Gadrat,[38] I. Garishvili,[61] F. Gastineau,[60] M. Germain,[60] A. Glenn,[11,36,61] H. Gong,[59] M. Gonin,[35] J. Gosset,[14] Y. Goto,[52,53] R. Granier de Cassagnac,[35] N. Grau,[12,26] S. V. Greene,[64] G. Grim,[37] M. Grosse Perdekamp,[23,53] T. Gunji,[10] H.-Å. Gustafsson,[39,*] T. Hachiya,[21,52] A. Hadj Henni,[60] C. Haegemann,[46] J. S. Haggerty,[5] M. N. Hagiwara,[1] K. I. Hahn,[17] H. Hamagaki,[10] J. Hamblen,[61] R. Han,[50] J. Hanks,[12] H. Harada,[21] E. P. Hartouni,[36] K. Haruna,[21] M. Harvey,[5] E. Haslum,[39] K. Hasuko,[52] R. Hayano,[10] X. He,[20] M. Heffner,[36] T. K. Hemmick,[59] T. Hester,[6] J. M. Heuser,[52] H. Hiejima,[23] J. C. Hill,[26] R. Hobbs,[46] M. Hohlmann,[18] M. Holmes,[64] W. Holzmann,[12,58] K. Homma,[21] B. Hong,[32] T. Horaguchi,[21,52,62] D. Hornback,[61] S. Huang,[64] M. G. Hur,[29] T. Ichihara,[52,53] R. Ichimiya,[52] J. Ide,[43] H. Iinuma,[34,52] Y. Ikeda,[63] K. Imai,[34,52] M. Inaba,[63] Y. Inoue,[52,54] D. Isenhower,[1] L. Isenhower,[1] M. Ishihara,[52] T. Isobe,[10] M. Issah,[58,64] A. Isupov,[27] D. Ivanischev,[51] Y. Iwanaga,[21] B. V. Jacak,[59,†] J. Jia,[5,12,58] X. Jiang,[37] J. Jin,[12] O. Jinnouchi,[53] B. M. Johnson,[5] T. Jones,[1] K. S. Joo,[44] D. Jouan,[49] D. S. Jumper,[1] F. Kajihara,[10,52] S. Kametani,[10,52,65] N. Kamihara,[52,53,62] J. Kamin,[59] M. Kaneta,[53] J. H. Kang,[67] H. Kanou,[52,62] J. Kapustinsky,[37] K. Karatsu,[34] M. Kasai,[52,54] T. Kawagishi,[63] D. Kawall,[41,53] M. Kawashima,[54,52] A. V. Kazantsev,[33] S. Kelly,[11] T. Kempel,[26] A. Khanzadeev,[51] K. M. Kijima,[21] J. Kikuchi,[65] A. Kim,[17] B. I. Kim,[32] D. H. Kim,[44] D. J. Kim,[28,67] E. Kim,[57] E. J. Kim,[8] S. H. Kim,[67] Y.-J. Kim,[23] Y.-S. Kim,[29] Y. J. Kim,[23] E. Kinney,[11] K. Kiriluk,[11] Á. Kiss,[16] E. Kistenev,[5] A. Kiyomichi,[52] J. Klay,[36] C. Klein-Boesing,[42] L. Kochenda,[51] V. Kochetkov,[22] B. Komkov,[51] M. Konno,[63] J. Koster,[23] D. Kotchetkov,[6,46] A. Kozlov,[66] A. Král,[13] A. Kravitz,[12] P. J. Kroon,[5] J. Kubart,[7,25] G. J. Kunde,[37] N. Kurihara,[10] K. Kurita,[52,54] M. Kurosawa,[52] M. J. Kweon,[32] Y. Kwon,[61,67] G. S. Kyle,[47] R. Lacey,[58] Y. S. Lai,[12] J. G. Lajoie,[26] A. Lebedev,[26] Y. Le Bornec,[49] S. Leckey,[59] D. M. Lee,[37] J. Lee,[17] K. Lee,[57] K. B. Lee,[32] K. S. Lee,[32] M. K. Lee,[67] T. Lee,[57] M. J. Leitch,[37] M. A. L. Leite,[56] E. Leitner,[64] B. Lenzi,[56] X. Li,[9] X. H. Li,[6] P. Lichtenwalner,[43] P. Liebing,[53] H. Lim,[57] L. A. Linden Levy,[11] T. Liška,[13] A. Litvinenko,[27] H. Liu,[37,47] M. X. Liu,[37] B. Love,[64] R. Luechtenborg,[42] D. Lynch,[5] C. F. Maguire,[64] Y. I. Makdisi,[4,5] A. Malakhov,[27] M. D. Malik,[46] V. I. Manko,[33] E. Mannel,[12] Y. Mao,[50,52] L. Mašek,[7,25] H. Masui,[63] F. Matathias,[12,59] M. C. McCain,[23] M. McCumber,[59] P. L. McGaughey,[37] N. Means,[59] B. Meredith,[23] Y. Miake,[63] T. Mibe,[30] A. C. Mignerey,[40] P. Mikeš,[7,25] K. Miki,[52,63] T. E. Miller,[64] A. Milov,[5,59] S. Mioduszewski,[5] G. C. Mishra,[20] M. Mishra,[2] J. T. Mitchell,[5] M. Mitrovski,[58] A. K. Mohanty,[3] H. J. Moon,[44] Y. Morino,[10] A. Morreale,[6] D. P. Morrison,[5] J. M. Moss,[37] T. V. Moukhanova,[33] D. Mukhopadhyay,[64] T. Murakami,[34] J. Murata,[52,54] S. Nagamiya,[30] Y. Nagata,[63] J. L. Nagle,[11] M. Naglis,[66] M. I. Nagy,[16,31] I. Nakagawa,[52,53] Y. Nakamiya,[21] K. R. Nakamura,[34] T. Nakamura,[21,30,52] K. Nakano,[52,62] S. Nam,[17] J. Newby,[36] M. Nguyen,[59] M. Nihashi,[21] B. E. Norman,[37] R. Nouicer,[5] A. S. Nyanin,[33] J. Nystrand,[39] C. Oakley,[20] E. O'Brien,[5] S. X. Oda,[10] C. A. Ogilvie,[26] H. Ohnishi,[52] I. D. Ojha,[64] M. Oka,[63] K. Okada,[53] O. O. Omiwade,[1] Y. Onuki,[52] A. Oskarsson,[39] I. Otterlund,[39] M. Ouchida,[21,52] K. Ozawa,[10] R. Pak,[5] D. Pal,[64] A. P. T. Palounek,[37] V. Pantuev,[24,59] V. Papavassiliou,[47] I. H. Park,[17] J. Park,[57] S. K. Park,[32] W. J. Park,[32] S. F. Pate,[47] H. Pei,[26] J.-C. Peng,[23] H. Pereira,[14] V. Peresedov,[27] D.Yu. Peressounko,[33] R. Petti,[59] C. Pinkenburg,[5] R. P. Pisani,[5] M. Proissl,[59] M. L. Purschke,[5] A. K. Purwar,[37,59] H. Qu,[20] J. Rak,[26,28,46] A. Rakotozafindrabe,[35] I. Ravinovich,[66] K. F. Read,[48,61] S. Rembeczki,[18] M. Reuter,[59] K. Reygers,[42] V. Riabov,[51] Y. Riabov,[51] E. Richardson,[40] D. Roach,[64] G. Roche,[38] S. D. Rolnick,[6] A. Romana,[35,*] M. Rosati,[26] C. A. Rosen,[11] S. S. E. Rosendahl,[39] P. Rosnet,[38] P. Rukoyatkin,[27] P. Ružička,[25] V. L. Rykov,[52] S. S. Ryu,[67] B. Sahlmueller,[42] N. Saito,[30,34,52,53] T. Sakaguchi,[5,10,65] S. Sakai,[63] K. Sakashita,[52,62] H. Sakata,[21] V. Samsonov,[51] S. Sano,[10,65] H. D. Sato,[34,52] S. Sato,[5,30,63] T. Sato,[63] S. Sawada,[30] K. Sedgwick,[6] J. Seele,[11] R. Seidl,[23,53] A.Yu. Semenov,[26] V. Semenov,[22] R. Seto,[6] D. Sharma,[66] T. K. Shea,[5] I. Shein,[22] A. Shevel,[51,58] T.-A. Shibata,[52,62] K. Shigaki,[21] M. Shimomura,[63] T. Shohjoh,[63] K. Shoji,[34,52] P. Shukla,[3] A. Sickles,[5,59] C. L. Silva,[26,56] D. Silvermyr,[48] C. Silvestre,[14] K. S. Sim,[32] B. K. Singh,[2] C. P. Singh,[2] V. Singh,[2] S. Skutnik,[26] M. Slunečka,[7,27] W. C. Smith,[1] A. Soldatov,[22] R. A. Soltz,[36] W. E. Sondheim,[37] S. P. Sorensen,[61] I. V. Sourikova,[5] N. A. Sparks,[1] F. Staley,[14] P. W. Stankus,[48] E. Stenlund,[39] M. Stepanov,[47] A. Ster,[31] S. P. Stoll,[5] T. Sugitate,[21]

C. Suire,[49] A. Sukhanov,[5] J. P. Sullivan,[37] J. Sziklai,[31] T. Tabaru,[53] S. Takagi,[63] E. M. Takagui,[56] A. Taketani,[52,53] R. Tanabe,[63] K. H. Tanaka,[30] Y. Tanaka,[45] S. Taneja,[59] K. Tanida,[34,52,53,57] M. J. Tannenbaum,[5] S. Tarafdar,[2] A. Taranenko,[58] P. Tarján,[15] H. Themann,[59] D. Thomas,[1] T. L. Thomas,[46] M. Togawa,[34,52,53] A. Toia,[59] J. Tojo,[52] L. Tomášek,[25] H. Torii,[21,52] R. S. Towell,[1] V-N. Tram,[35] I. Tserruya,[66] Y. Tsuchimoto,[21,52] S. K. Tuli,[2,*] H. Tydesjö,[39] N. Tyurin,[22] C. Vale,[5,26] H. Valle,[64] H. W. van Hecke,[37] E. Vazquez-Zambrano,[12] A. Veicht,[23] J. Velkovska,[64] R. Vértesi,[15,31] A. A. Vinogradov,[33] M. Virius,[13] V. Vrba,[25] E. Vznuzdaev,[51] M. Wagner,[34,52] D. Walker,[59] X. R. Wang,[47] D. Watanabe,[21] K. Watanabe,[63] Y. Watanabe,[52,53] F. Wei,[26] R. Wei,[58] J. Wessels,[42] S. N. White,[5] N. Willis,[49] D. Winter,[12] J. P. Wood,[1] C. L. Woody,[5] R. M. Wright,[1] M. Wysocki,[11] W. Xie,[6,53] Y. L. Yamaguchi,[10,65] K. Yamaura,[21] R. Yang,[23] A. Yanovich,[22] Z. Yasin,[6] J. Ying,[20] S. Yokkaichi,[52,53] Z. You,[50] G. R. Young,[48] I. Younus,[46] I. E. Yushmanov,[33] W. A. Zajc,[12] O. Zaudtke,[42] C. Zhang,[12,48] S. Zhou,[9] J. Zimányi,[31,*] and L. Zolin[27]

(PHENIX Collaboration)

[1]*Abilene Christian University, Abilene, Texas 79699, USA*
[2]*Department of Physics, Banaras Hindu University, Varanasi 221005, India*
[3]*Bhabha Atomic Research Centre, Bombay 400 085, India*
[4]*Collider Accelerator Department, Brookhaven National Laboratory, Upton, New York 11973-5000, USA*
[5]*Physics Department, Brookhaven National Laboratory, Upton, New York 11973-5000, USA*
[6]*University of California-Riverside, Riverside, California 92521, USA*
[7]*Charles University, Ovocný trh 5, Praha 1, 116 36, Prague, Czech Republic*
[8]*Chonbuk National University, Jeonju, 561-756, Korea*
[9]*Science and Technology on Nuclear Data Laboratory, China Institute of Atomic Energy, Beijing 102413, P. R. China*
[10]*Center for Nuclear Study, Graduate School of Science, University of Tokyo, 7-3-1 Hongo, Bunkyo, Tokyo 113-0033, Japan*
[11]*University of Colorado, Boulder, Colorado 80309, USA*
[12]*Columbia University, New York, New York 10027 and Nevis Laboratories, Irvington, New York 10533, USA*
[13]*Czech Technical University, Zikova 4, 166 36 Prague 6, Czech Republic*
[14]*Dapnia, CEA Saclay, F-91191, Gif-sur-Yvette, France*
[15]*Debrecen University, H-4010 Debrecen, Egyetem tér 1, Hungary*
[16]*ELTE, Eötvös Loránd University, H-1117 Budapest, Pázmány P. s. 1/A, Hungary*
[17]*Ewha Womans University, Seoul 120-750, Korea*
[18]*Florida Institute of Technology, Melbourne, Florida 32901, USA*
[19]*Florida State University, Tallahassee, Florida 32306, USA*
[20]*Georgia State University, Atlanta, Georgia 30303, USA*
[21]*Hiroshima University, Kagamiyama, Higashi-Hiroshima 739-8526, Japan*
[22]*IHEP Protvino, State Research Center of Russian Federation, Institute for High Energy Physics, Protvino, 142281, Russia*
[23]*University of Illinois at Urbana-Champaign, Urbana, Illinois 61801, USA*
[24]*Institute for Nuclear Research of the Russian Academy of Sciences, prospekt 60-letiya Oktyabrya 7a, Moscow 117312, Russia*
[25]*Institute of Physics, Academy of Sciences of the Czech Republic, Na Slovance 2, 182 21 Prague 8, Czech Republic*
[26]*Iowa State University, Ames, Iowa 50011, USA*
[27]*Joint Institute for Nuclear Research, 141980 Dubna, Moscow Region, Russia*
[28]*Helsinki Institute of Physics and University of Jyväskylä, P.O.Box 35, FI-40014 Jyväskylä, Finland*
[29]*KAERI, Cyclotron Application Laboratory, Seoul, Korea*
[30]*KEK, High Energy Accelerator Research Organization, Tsukuba, Ibaraki 305-0801, Japan*
[31]*KFKI Research Institute for Particle and Nuclear Physics of the Hungarian Academy of Sciences (MTA KFKI RMKI), H-1525 Budapest 114, POBox 49, Budapest, Hungary*
[32]*Korea University, Seoul, 136-701, Korea*
[33]*Russian Research Center "Kurchatov Institute," Moscow, 123098 Russia*
[34]*Kyoto University, Kyoto 606-8502, Japan*
[35]*Laboratoire Leprince-Ringuet, Ecole Polytechnique, CNRS-IN2P3, Route de Saclay, F-91128, Palaiseau, France*
[36]*Lawrence Livermore National Laboratory, Livermore, California 94550, USA*
[37]*Los Alamos National Laboratory, Los Alamos, New Mexico 87545, USA*
[38]*LPC, Université Blaise Pascal, CNRS-IN2P3, Clermont-Fd, 63177 Aubiere Cedex, France*
[39]*Department of Physics, Lund University, Box 118, SE-221 00 Lund, Sweden*
[40]*University of Maryland, College Park, Maryland 20742, USA*
[41]*Department of Physics, University of Massachusetts, Amherst, Massachusetts 01003-9337, USA*
[42]*Institut fur Kernphysik, University of Muenster, D-48149 Muenster, Germany*
[43]*Muhlenberg College, Allentown, Pennsylvania 18104-5586, USA*
[44]*Myongji University, Yongin, Kyonggido 449-728, Korea*
[45]*Nagasaki Institute of Applied Science, Nagasaki-shi, Nagasaki 851-0193, Japan*
[46]*University of New Mexico, Albuquerque, New Mexico 87131, USA*

[47]*New Mexico State University, Las Cruces, New Mexico 88003, USA*

[48]*Oak Ridge National Laboratory, Oak Ridge, Tennessee 37831, USA*

[49]*IPN-Orsay, Universite Paris Sud, CNRS-IN2P3, BP1, F-91406, Orsay, France*

[50]*Peking University, Beijing 100871, P. R. China*

[51]*PNPI, Petersburg Nuclear Physics Institute, Gatchina, Leningrad region, 188300, Russia*

[52]*RIKEN Nishina Center for Accelerator-Based Science, Wako, Saitama 351-0198, Japan*

[53]*RIKEN BNL Research Center, Brookhaven National Laboratory, Upton, New York 11973-5000, USA*

[54]*Physics Department, Rikkyo University, 3-34-1 Nishi-Ikebukuro, Toshima, Tokyo 171-8501, Japan*

[55]*Saint Petersburg State Polytechnic University, St. Petersburg, 195251 Russia*

[56]*Universidade de São Paulo, Instituto de Física, Caixa Postal 66318, São Paulo CEP05315-970, Brazil*

[57]*Seoul National University, Seoul, Korea*

[58]*Chemistry Department, Stony Brook University, SUNY, Stony Brook, New York 11794-3400, USA*

[59]*Department of Physics and Astronomy, Stony Brook University, SUNY, Stony Brook, New York 11794-3400, USA*

[60]*SUBATECH (Ecole des Mines de Nantes, CNRS-IN2P3, Université de Nantes) BP 20722-44307, Nantes, France*

[61]*University of Tennessee, Knoxville, Tennessee 37996, USA*

[62]*Department of Physics, Tokyo Institute of Technology, Oh-okayama, Meguro, Tokyo 152-8551, Japan*

[63]*Institute of Physics, University of Tsukuba, Tsukuba, Ibaraki 305, Japan*

[64]*Vanderbilt University, Nashville, Tennessee 37235, USA*

[65]*Waseda University, Advanced Research Institute for Science and Engineering, 17 Kikui-cho, Shinjuku-ku, Tokyo 162-0044, Japan*

[66]*Weizmann Institute, Rehovot 76100, Israel*

[67]*Yonsei University, IPAP, Seoul 120-749, Korea*

The PHENIX experiment at the Relativistic Heavy Ion Collider has measured ω meson production via leptonic and hadronic decay channels in $p + p$, $d +$ Au, Cu + Cu, and Au + Au collisions at $\sqrt{s_{NN}} = 200$ GeV. The invariant transverse momentum spectra measured in different decay modes give consistent results. Measurements in the hadronic decay channel in Cu + Cu and Au + Au collisions show that ω production has a suppression pattern at high transverse momentum, similar to that of π^0 and η in central collisions, but no suppression is observed in peripheral collisions. The nuclear modification factors, R_{AA}, are consistent in Cu + Cu and Au + Au collisions at similar numbers of participant nucleons.

I. INTRODUCTION

The measurement of hadrons produced in relativistic heavy-ion collisions is a well established tool in the study of the hot and dense matter created in the collisions. The PHENIX experiment at the Relativistic Heavy Ion Collider has carried out systematic measurement of hadrons in $p + p$, $d +$ Au, Cu + Cu, and Au + Au collisions at $\sqrt{s_{NN}} = 200$ GeV. When compared to existing measurements in $p + p$ and $d +$ Au, measurements in heavy-ion collisions suggest that particle production at high p_T is affected by jet quenching, which is considered to be an effect of extremely dense matter created by the collisions [1]. High p_T suppression of π^0 and η was measured in Cu + Cu and Au + Au [2–5] and the nuclear modification factors (R_{AA}) of these mesons were found to be consistent with each other in p_T and centrality. A comparison with theoretical models was first done for π^0 suppression in [4], with the result that the suppression increases proportional to the number of participating nucleons as $N_{part}^{2/3}$. This result is consistent with existing energy loss models such as the Parton Quenching Model (PQM) [6].

The ω meson comprises light valence quarks similar to the π^0 and η but has a larger mass (782 MeV) and a spin [1]. These differences make the omega measurement an additional probe to a systematic study to understand mechanisms of parton energy loss and hadron production in the collisions. The p_T dependence of the particle production ratio (ω/π) and the nuclear modification factors (R_{AA}) should add information about the parton energy loss mechanism. Furthermore, using multiple decay channels: a leptonic channel $\omega \rightarrow e^+e^-$ (with branching ratio BR $= 7.18 \pm 0.12 \times 10^{-5}$) and two hadronic decay channels $\omega \rightarrow \pi^+\pi^-\pi^0$ (BR $= (89.1 \pm 0.7) \times 10^{-2}$) and $\omega \rightarrow \pi^0\gamma$ (BR $= (8.90 + 0.27 - 0.23) \times 10^{-2}$) [9] extends the p_T range by using the hadronic channels at high p_T and the leptonic channel at low p_T.

Baseline measurements of the ω have been performed for $p + p$ via the leptonic channel [7] and for the $p + p$ and $d +$Au in the hadronic channel [8,10]. The ω/π^0 ratio was found to be independent of transverse momentum and equal to $0.85 \pm 0.05^{\text{stat}} \pm 0.09^{\text{syst}}$ in $p + p$ and $0.94 \pm 0.08^{\text{stat}} \pm 0.12^{\text{syst}}$ in $d +$Au collisions for $p_T > 2$ GeV/c [8].

This article presents the first measurements of ω meson production in Cu + Cu and Au + Au collisions at PHENIX via the $\pi^0\gamma$ channel. These measurements permit the study of ω suppression at high p_T. This paper also presents measurements of the ω meson in $d +$ Au collisions with significantly reduced uncertainties in the hadronic channel and a first measurement in the dielectronic channel.

II. EXPERIMENTAL SETUP

The PHENIX experiment is designed specifically to measure electromagnetic probes such as electrons, muons, and photons [11]. The detectors of the PHENIX experiment can be grouped into three categories: inner detectors close to the beam pipe, two central arms with pseudorapidity coverage of ± 0.35, each covering 90 degrees in azimuthal angle, and two muon detectors, which have 2π azimuthal and pseudorapidity coverage of $+(1.2$–$2.2)$ for the south muon arm and $-(1.2$–$2.4)$ for the north muon arm. The central arms are used to measure the ω mesons at midrapidity.

The inner detectors are used for triggering, measurement of the z coordinate of the collision vertex, and centrality of the interactions with beam-beam counters (BBC) and zero-degree calorimeters (ZDC). The central arms are capable of measuring a variety of particles by using drift chambers and pad chambers for tracking and momentum measurement of charged particles, ring imaging Čerenkov detectors (RICH) for the separation of electrons up to the π Čerenkov threshold at 4 GeV/c, and an electromagnetic calorimeter (EMCal) for the measurement of spatial positions and energies of photons and electrons. The EMCal comprises six sectors of lead-scintillator calorimeter and two sectors of lead-glass calorimeter. Additional details of the PHENIX experimental setup and performance of the detector subsystems can be found elsewhere [7,12].

We used data samples collected in 2004, 2005, 2007, and 2008 as summarized in Table I. The data were taken using a minimum bias trigger (MB) and the EMCal-RICH-trigger (ERT), which is described below. The 2003 $d + \mathrm{Au}$ data were published in Ref. [8] and are included here for comparison. The 2005 $p + p$ data were published in Ref. [7] and are used as the baseline for R_{AA} in $d + \mathrm{Au}$, $\mathrm{Cu} + \mathrm{Cu}$, and $\mathrm{Au} + \mathrm{Au}$. Two $\mathrm{Au} + \mathrm{Au}$ data samples were taken in 2004 and 2007. The MB trigger required a coincidence between the north and south BBC [13]. In the $\mathrm{Au} + \mathrm{Au}$ data sample taken in 2004, additional coincidence between the ZDC and BBC was required. To enhance the statistics at high p_T, the ERT trigger was used for $p + p$, $d + \mathrm{Au}$, and $\mathrm{Cu} + \mathrm{Cu}$ data taking, which required the event to satisfy the MB trigger conditions and that there be at least one high-p_T electron or photon candidate

in the event. For electron candidates the ERT trigger required a minimum energy deposit of 0.4 (0.6 and 0.8) GeV/c in a tile of 2×2 EMCal towers matched to a hit in the RICH in $p + p$ ($d + \mathrm{Au}$) collisions. For the photon candidates, the ERT trigger required a minimum energy deposit of 1.4, 2.4, and 3.4 GeV/c in a tile of 4×4 EMCal towers in $p + p$, $d + \mathrm{Au}$, and $\mathrm{Cu} + \mathrm{Cu}$ collisions, respectively. In the $d + \mathrm{Au}$ and the $\mathrm{Cu} + \mathrm{Cu}$ analysis, the MB data set was used to measure ω production up to 4 GeV/c in $d + \mathrm{Au}$ and 6 GeV/c in $\mathrm{Cu} + \mathrm{Cu}$; the ERT sample was used at higher p_T. The ERT trigger efficiencies measured for single photons and electrons and calculated for ω mesons is described in Sec. III D.

III. DATA ANALYSIS

In this section, we describe the event selection and data analysis for reconstructing the leptonic ($\omega \to e^+e^-$) and hadronic ($\omega \to \pi^+\pi^-\pi^0$ and $\omega \to \pi^0\gamma$) decay channels of the ω. Corrections applied to the raw data to calculate the ω meson invariant yields and systematic uncertainties related to the measurements are also presented.

A. Event selection and basic analysis cut

For data taken in 2004, the correlation of the charge deposited in the BBCs with energy deposited in the ZDCs provides a determination of the centrality of the collisions. For data taken in 2005, 2007, and 2008, the centralities were only determined by using BBC. A Glauber Monte Carlo [14] with the BBC and ZDC responses was used to estimate the number of binary nucleon-nucleon collisions (N_{coll}) and the number of participating collisions (N_{part}) for each centrality bin [15].

Events are selected with a reconstructed z vertex within 30 cm of the center of the interaction region. Charged tracks were required to have momenta in the range of $0.2 < p_T < 5.0$ (7.0) GeV/c for the $\omega \to e^+e^-$ analysis in $p + p$ ($d + \mathrm{Au}$) [7] and $0.3 < p_T < 8.0$ GeV/c for the $\omega \to \pi^+\pi^-\pi^0$ decay channel [8]. Charged particles with $p_T < 0.2$ GeV/c have a large bending angle in the axial magnetic field of the PHENIX central magnet [16] and most of them do not pass

TABLE I. Summary of the analyzed data samples and ω meson decay channels. Values for previously published PHENIX data (PRD83) [7] and (PRC75) [8] are given for comparison. Threshold refers to the thresholds for electron or photon candidates, which is discussed in text.

Data set	Trigger	Sampled events	$\int L dt$	Threshold	Decay channel	Reference
2003 $d + \mathrm{Au}$	ERT	5.5B	2.74 nb^{-1}	2.4 GeV	$\omega \to \pi^+\pi^-\pi^0$	PRC75 [8]
				2.4 GeV	$\omega \to \pi^0\gamma$	PRC75 [8]
2004 $\mathrm{Au} + \mathrm{Au}$	MB	1.5B	241 μb^{-1}	N/A	$\omega \to \pi^0\gamma$	This work
2005 $p + p$	ERT	85B	3.78 pb^{-1}	0.4 GeV	$\omega \to e^+e^-$	PRD83 [7]
				1.4 GeV	$\omega \to \pi^+\pi^-\pi^0$	PRD83 [7]
				1.4 GeV	$\omega \to \pi^0\gamma$	PRD83 [7]
2005 $\mathrm{Cu} + \mathrm{Cu}$	MB	8.6B	3.06 pb^{-1}	N/A	$\omega \to \pi^0\gamma$	This work
	ERT			3.4 GeV	$\omega \to \pi^0\gamma$	This work
2007 $\mathrm{Au} + \mathrm{Au}$	MB	5.1B	813 μb^{-1}	N/A	$\omega \to \pi^0\gamma$	This work
2008 $d + \mathrm{Au}$	ERT	160B	80 nb^{-1}	0.6/0.8 GeV	$\omega \to e^+e^-$	This work
				2.4 GeV	$\omega \to \pi^+\pi^-\pi^0$	This work
				2.4 GeV	$\omega \to \pi^0\gamma$	This work

through the entire tracking system. Electrons and positrons are identified mainly by the Čerenkov photons emitted in the RICH by requiring at least two photomultipliers hit in the RICH cells matched to the track [17]. Also, matching of the energy measured for the charged track in the EMCal with the momentum measured in the tracking system, $|E/p - 1| < 0.5$, helps to further improve e/π separation. Together the RICH and EMCal provide an e/π rejection factor of about $1:10^4$. Photon identification is performed by the shower shape criteria in the EMCal [18], and the energy of the selected γ clusters is above 0.2 GeV.

B. Leptonic analysis

The leptonic analysis is done only in $p + p$ and $d + $Au. In case of $\omega \to e^+e^-$, all electrons and positrons reconstructed in each event are combined into pairs, resulting in signal peaks that sit on top of a combinatorial background in the invariant mass distribution. The uncorrelated part of the background is estimated with an event-mixing technique, which combines tracks from different events with similar event centrality and z coordinate of the collision vertex. Details of the event mixing procedure are presented in Ref. [19].

Figure 1 shows invariant mass spectra of e^+e^- pairs in $p + p$ and $d + $Au collisions at $\sqrt{s_{NN}} = 200$ GeV after subtraction of combinatorial background as described above. The solid lines show the global fits which include: (1) contributions from ω, ρ, and ϕ mesons approximated with Breit-Wigner functions convolved with Gaussian distributions to account for the detector mass resolution; masses and widths of the ω, ρ, and ϕ are fixed to the PDG values; the ρ component is calculated assuming that ω and ρ have the same yield and vacuum branching ratios; (2) other correlated residual background, which is dominated by a contribution from jets, is approximated by a second-order polynomial function. The detector resolution, which is determined from simulations, is found to be dependent on mass and momentum and varies from 6 to 18 MeV/c^2.

The ω yield is determined by counting bin contents in a 3 σ width (derived from the fitting) and subtracting the polynomial background. An associated systematic uncertainty from the raw yield extraction is calculated by varying the background normalization, fitting functions, range, and counting methods. The estimated value is 4–15% in $p + p$ [7] and 8–15% in $d + $Au collisions.

C. Hadronic analysis

In the $\omega \to \pi^+\pi^-\pi^0$ and $\omega \to \pi^0\gamma$ channels, the first analysis step is to reconstruct π^0 mesons by combining pairs of photons reconstructed in an event. Then the mass and width of the π^0 peak in the invariant mass distribution of photon pairs are parametrized as a function of transverse momentum. The 1 σ width of the π^0 peak varies from 13 to 9 MeV/c^2 as p_T increases from 1 to 4 GeV/c and is determined by the EMCal energy resolution. A pair of photons is selected as a π^0 candidate if its invariant mass is within 2 σ of the reconstructed π^0 mass. In Cu + Cu and Au + Au, an additional asymmetry cut for π^0 candidates is used to reduce combinatorial background,
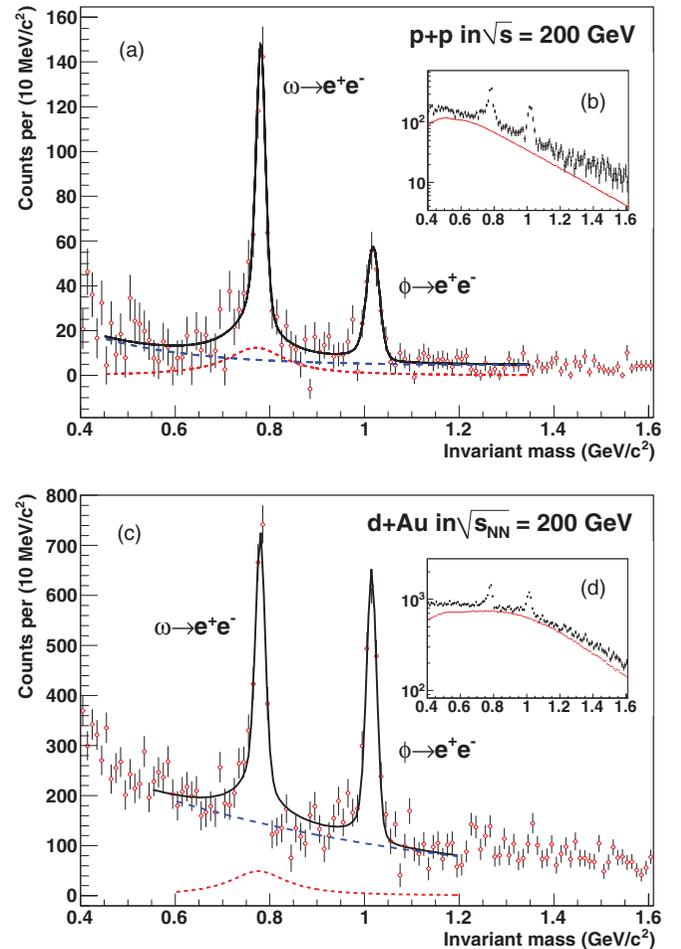

FIG. 1. (Color online) Invariant mass of e^+e^- pairs detected by the PHENIX central arms with uncorrelated combinatorial background subtracted (see text) for (a) $p + p$ collisions and (c) minimum-bias $d + $Au collisions at $\sqrt{s_{NN}} = 200$ GeV and integrated over p_T. Inserts (b) and (d) show the raw spectra before subtraction. The spectrum is fit to the ω and ϕ resonances where the masses and widths are set to the PDG values; the Breit-Wigner resonance shape is convolved with a Gaussian to account for detector mass resolution estimated from simulation and then corrected for the radiative tail. The ρ contribution is shown as the dotted (red) line with an assumption that the yield is the same as that of the ω. The residual continuum component is estimated by a polynomial fit as shown by the dashed (blue) line.

$\alpha = |E_{\gamma_1} - E_{\gamma_2}|/|E_{\gamma_1} + E_{\gamma_2}| < 0.8$. Selected π^0 candidates, which include true π^0s and combinatorial background are combined either with the third photon with energy $E_\gamma > 1.0$ GeV/c for the $\omega \to \pi^0\gamma$ or with a pair of opposite-sign charged tracks for the $\omega \to \pi^+\pi^-\pi^0$ decay.

In the $p + p$ and $d + $Au analysis, the ω meson raw yields are extracted by fitting the p_T slices of the invariant mass distribution with a combination of a Gaussian for the signal and a second order polynomial for the background. The width and mass of the reconstructed ω mesons were found to be in good agreement with values expected from simulation. Details of these analyses are described in Ref. [10].
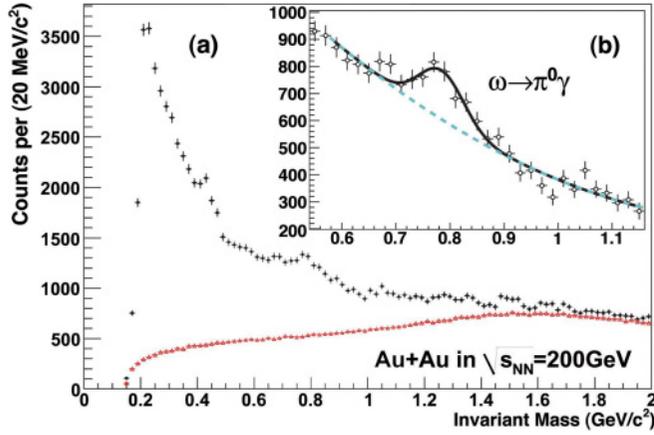
FIG. 2. (Color online) (a) Invariant mass and scaled mixed background distributions for $\pi^0\gamma$ decay at $7 < p_T < 12$ GeV/c in Au + Au collisions. (b) Invariant mass distribution after subtraction of scaled background.
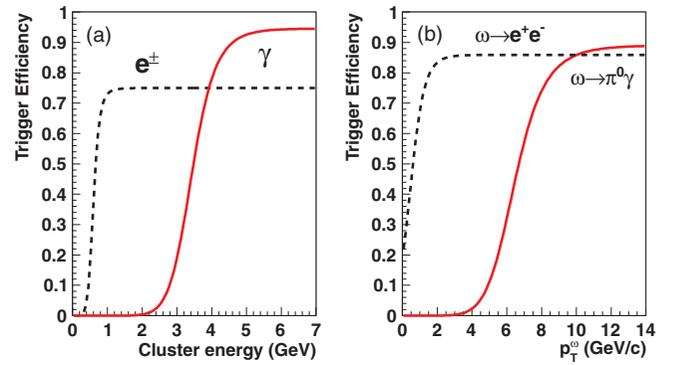

FIG. 3. (Color online) Typical ERT trigger efficiencies for (a) single electrons (0.6 GeV threshold) and photons (3.4 GeV threshold) and (b) $\omega \to e^+e^-$ and $\omega \to \pi^0\gamma$ using corresponding triggered electrons/photons.

In the Cu + Cu and Au + Au analysis, only the $\omega \to \pi^0\gamma$ channel was analyzed due to high combinatorial background in the $\omega \to \pi^+\pi^-\pi^0$ channel. The uncorrelated combinatorial background was estimated using an event mixing technique where the third photon in the $\pi^0\gamma$ decay was taken from the different events with a similar centrality and z vertex. For every p_T bin, before subtraction, the calculated background was normalized to match the integral of the foreground at an invariant mass $1.75 < M_{\text{inv}} < 4.0$ GeV/c^2, over which we expect the contribution from correlated background to be small. An example of the invariant mass distribution and normalized background distributions is shown in Fig. 2(a) and the invariant mass distribution after subtraction shown in Fig. 2(b). The resulting invariant mass distribution contains residual background from correlated particles: the background contributions are from $K_s \to \pi^0\pi^0$ decays, and π^0 and η, where one of the photons from $\pi^0(\eta) \to \gamma\gamma$ decay creates a fake π^0 candidate for the $\omega \to \pi^0\gamma$ reconstruction. The $\omega \to \pi^0\gamma$ peak is further enhanced by a mixed background subtraction. Finally, raw yields of ω are extracted by fitting the spectra with a combination of a Gaussian and a polynomial. The width of the Gaussian used in the fit to the data is limited to ± 1 MeV/c^2 around the value determined from simulation. The ω yield is calculated as an integral of the Gaussian.

Systematic uncertainties associated with the raw yield extraction are evaluated using different fitting functions and ranges, different counting methods and kinematic cuts, varying the EMCal resolution in simulation, and applying different limits for the width of ω peaks in fits to data. The estimated value is 13–35% in Cu + Cu and 20–35% in Au + Au collisions.

D. Reconstruction efficiencies

The reconstruction efficiency of the ω is determined using a GEANT simulation of the PHENIX detector tuned to reproduce the performance of the detector subsystems. The ω mesons are generated and decayed into corresponding decay channels

and reconstructed with the same analysis chain as the real data. The generated ω spectra were weighted to match the measured particle spectra. It was verified that the simulated positions and widths of the reconstructed particle peaks are consistent with the values measured in real data.

The reconstruction efficiency is divided into three components: ϵ, ϵ_{trig}, and ϵ_{emb}. The efficiency ϵ is the reconstruction efficiency for minimum bias events in a low-occupancy environment, like in $p + p$ and $d + $Au collisions. This efficiency accounts for the limited geometrical acceptance, resolution, and efficiencies of the detector subsystems as well as for analysis cuts. When a selective ERT trigger is used, an additional trigger efficiency factor, ϵ_{trig}, is applied. This factor measures the efficiency of the ERT trigger logic. For higher multiplicity collisions, one needs to account for the loss of efficiency from increased detector occupancy: this is measured through the embedding efficiency ϵ_{emb}. A measured raw yield then needs to be corrected for the total efficiency $\epsilon \times \epsilon_{\text{emb}} \times \epsilon_{\text{trig}}$, depending on the collision, centrality, and trigger involved.

The ERT data sample was used to measure dielectron and hadronic decay channels of the ω at high p_T in $p + p$, $d + $Au, and Cu + Cu. The threshold settings for ERT are described in Sec. II. The single particle ERT efficiency was measured by dividing the energy spectra of gamma clusters or electrons that fired the ERT trigger by the energy spectra of all clusters or electrons in the minimum bias data sample. Figure 3(a) shows a typical example of the ERT trigger efficiencies for single electrons and single photons as a function of cluster energy. The level of saturation of trigger efficiency curves is below 100% because of inactive areas of the ERT and the RICH detectors.

The ERT efficiencies for the ω meson in both the leptonic and hadronic decay modes were evaluated with the help of a Monte-Carlo simulation. For all fully reconstructed ω mesons, the calculated single photon or electron ERT efficiency curves were used to calculate the probability that one of the particles in the final state fires the ERT trigger. Figure 3(b) shows the corresponding trigger efficiencies for $\omega \to e^+e^-$ and $\omega \to \pi^0\gamma$. More detailed descriptions are presented in Refs. [7,10].
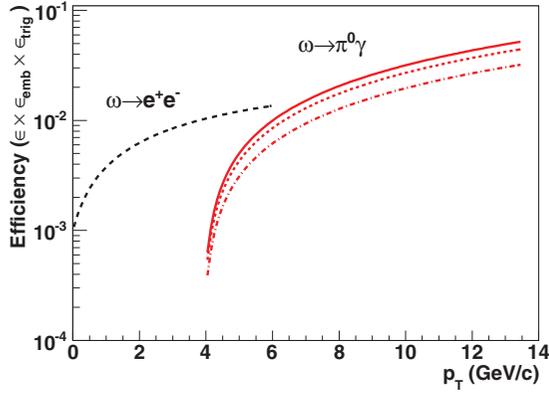
FIG. 4. (Color online) Typical reconstruction efficiencies for $\omega \to e^+e^-$ and $\omega \to \pi^0\gamma$. The curves for $\omega \to \pi^0\gamma$ include the embedding efficiency in Au + Au collisions: solid, dotted, and dot-dashed lines (red) are for 60–92%, 20–60%, and 0–20% centrality, respectively.

Figure 4 shows typical reconstruction efficiencies ϵ for $\omega \to e^+e^-$ and $\omega \to \pi^0\gamma$. In the case of Cu + Cu and Au + Au collisions, an additional efficiency correction $\epsilon_{\rm emb}$ due to cluster overlap in high multiplicity environment must be applied. In most central Au + Au events, the EMCal typically detects more than 300 clusters corresponding to a detector occupancy of $\sim$10%. To estimate the corresponding loss in efficiency, the simulated ω decays are embedded into real A + A events and analyzed. The merging effect results in $\sim$40% loss of reconstruction efficiency in 0–20% central Au + Au collisions, $\sim$15% loss in 0–20% central Cu + Cu collisions, and is almost negligible in peripheral collisions. Figure 4 shows the reconstruction efficiencies derived for Au + Au collisions at different centralities. Finally, in each bin we apply also a correction factor [7] to replace the average value of the yield in the analyzed p_T bin by the value of the yield in the middle of the bin.

E. Calculation of invariant yields

In $p + p$ and minimum bias $d + $ Au collisions, the invariant yield is related to the invariant cross section as:

$$E\frac{d^3\sigma}{dp^3} = \sigma_{pp}^{\rm inel}\left(\sigma_{d{\rm Au}}^{\rm inel}\right) \times \frac{1}{2\pi p_T N_{\rm evt}}\frac{d^2N}{dp_T dy}, \qquad (1)$$

where $\sigma_{pp}^{\rm inel}$ and $\sigma_{d{\rm Au}}^{\rm inel}$ are the total inelastic cross section, 42.2 and 2260 mb, respectively.

For a given centrality bin, the invariant yields as a function of p_T (invariant transverse momentum) are determined from:

$$\frac{1}{2\pi p_T}\frac{d^2N_{\rm cent}}{dp_T dy} \equiv \frac{1}{2\pi p_T N_{\rm cent}^{\rm evt}}\frac{1}{BR}\frac{1}{\epsilon(p_T)\epsilon_{\rm emb}(p_T,{\rm cent})\epsilon_{\rm trig}(p_T)}$$
$$\times \frac{N(\Delta p_T,{\rm cent})}{\Delta p_T \, \Delta y}, \qquad (2)$$

where $N_{\rm cent}^{\rm evt}$ is the number of events for a given centrality bin, $N(\Delta p_T,{\rm cent})$ is the raw yield of ω for each p_T and centrality bin, $\epsilon(p_T)$, $\epsilon_{\rm emb}(p_T,{\rm cent})$ and $\epsilon_{\rm trig}(p_T)$ are, as previously defined, reconstruction efficiency, embedding efficiency, and trigger efficiency, respectively. The trigger efficiency is applied

TABLE II. Summary of assigned systematic uncertainties of $\omega \to e^+e^-$ in $p + p$ and $d + $ Au analysis. (A), (B), and (C) refer to the uncertainty type, which is explained in text.

Source	$p + p$	$d + $ Au
Peak extraction	4–15%(A)	8.4–24.1%(A)
ERT efficiency	1–3%(B)	1–7%(B)
BBC cross section	9.7%(C)	7.9%(C)
Momentum scale	2–11%(B)	1.2–5.3%(B)
Acceptance correction	5%(B)	7%(B)
Electron ID	10%(B)	
Branching ratio	1.7%(C)	

only for the analyses using the ERT data set. BR is the decay branching ratio from Ref. [9], $(89.2 \pm 0.7 \times 10^{-2})$ for $\omega \to \pi^+\pi^-\pi^0$, $(8.90 \pm 0.27 \times 10^{-2})$ for $\omega \to \pi^0\gamma$, and $(7.16 \pm 0.12 \times 10^{-5})$ for $\omega \to e^+e^-$.

F. Systematic uncertainties

In addition to uncertainties related to the raw yield extraction described in the corresponding analysis sections, other sources of the uncertainties should also be taken into account. Uncertainties of the ERT trigger efficiency and acceptance corrections were estimated by varying the analysis cuts, energy, and momentum scales of the EMCal and drift chamber by $\sim$1% [7]. Uncertainties of detector response (mainly from the RICH for electron analysis and from the EMCal for hadronic analysis) are estimated by changing particle identification criteria in the analysis. A summary of assigned systematic uncertainties is listed in Table II for $\omega \to e^+e^-$ in $p + p$ and $d + $ Au and in Table III for $\omega \to \pi^0\gamma$ in Cu + Cu and Au + Au. Those are classified into three types: Type A is p_T-uncorrelated, Type B is p_T-correlated, and Type C is the overall normalization uncertainty. Total uncertainties for $\omega \to e^+e^-$ are 16–24% in $p + p$ [7] and 19–26% in $d + $ Au. The total uncertainties for $\omega \to \pi^0\gamma$ are 15–37% in Cu + Cu and 21–37% in Au + Au. Uncertainties for $\omega \to \pi^0\pi^+\pi^0$ analysis are 7–20% in $p + p$ and 10–15% in $d + $ Au, as described in Ref. [8].

TABLE III. Summary of assigned systematic uncertainties of $\omega \to \pi^0\gamma$ in Cu + Cu and Au + Au analysis. (A), (B), and (C) refer to the uncertainty type, which is explained in text.

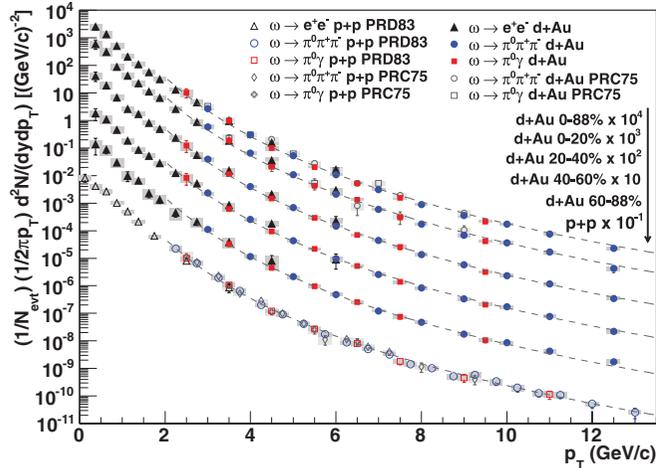| Source	Cu + Cu	Au + Au
Peak extraction	13–35%(A)	20.1–34.5%(A)
ERT efficiency	3–4%(B)	N/A
Energy scale		4–7%(B)
Energy resolution		2–3%(B)
Acceptance correction		3–6%(B)
Conversion		4.5%(C)
Branching ratio		3.4%(C)

FIG. 5. (Color online) Invariant transverse momentum spectra of ω production in $p + p$ and $d + \mathrm{Au}$ collisions at $\sqrt{s} = 200$ GeV. The dashed lines represent fits to $p + p$ results by a Tsallis distribution [20] scaled by the corresponding number of binary collisions for $d + \mathrm{Au}$. The previously published PHENIX data (PRD83) [7] and π^0 (PRC75) [8] are shown for comparison.

FIG. 6. Invariant transverse momentum spectra of ω production in (a) $\mathrm{Cu} + \mathrm{Cu}$ and (b) $\mathrm{Au} + \mathrm{Au}$ collisions from the $\omega \to \pi^0 \gamma$ decay channel for three centrality bins and minimum bias. The dashed lines are the $p + p$ results scaled by the corresponding number of binary collisions. The (a) $\mathrm{Cu} + \mathrm{Cu}$ data were recorded in 2005 and the (b) $\mathrm{Au} + \mathrm{Au}$ data were recorded in 2004 and 2007, as indicated.

IV. RESULTS

A. Invariant transverse momentum spectra

Figure 5 presents the invariant transverse momentum spectra measured for the ω meson in $p + p$ and $d + \mathrm{Au}$ at $\sqrt{s} = 200$ GeV. Previously published results are shown with open markers [8]. Results for different decay channels and data samples agree within uncertainties in the overlap region. The dashed curves in Fig. 5 are fixed on $p + p$ results at $p_T > 2$ GeV/c using a Tsallis distribution [20] and then scaled by the number of binary nucleon-nucleon collisions (N_{coll}) estimated using Glauber Monte-Carlo simulation [14] for $d + \mathrm{Au}$ results.

Figure 6 shows the invariant transverse momentum spectra measured for the ω meson in $\mathrm{Cu} + \mathrm{Cu}$ and $\mathrm{Au} + \mathrm{Au}$ collisions at $\sqrt{s_{NN}} = 200$ GeV. Measurements were performed only in the $\omega \to \pi^0 \gamma$ channel. Results are presented for three centrality bins: 0–20%, 20–60%, 60–92% (60–94% in $\mathrm{Cu} + \mathrm{Cu}$) and minimum bias collisions. The dashed lines represent N_{coll} scaled fits to $p + p$ results, where N_{coll} values were taken from [15] summarized in Table IV. The results show that in peripheral heavy ion collisions ω production generally follows binary scaling, while in midcentral and central collisions, production of ω mesons is suppressed at high p_T. Such behavior is similar to one previously observed for other light mesons [4,21] and can be attributed to medium-induced effects.

B. ω/π ratio

Measurement of ω production can be used to study the relative production of vector and pseudoscalar mesons consisting of the same valence quarks, i.e., ω/π ratio as a function of transverse momentum. In calculating the ω/π ratio,
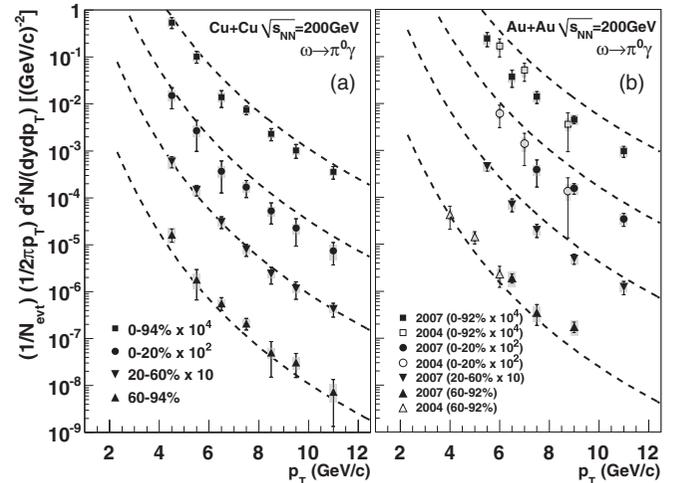
the same methodology from [4,22,23] for the π^+/π^- and π^0 was used. The charged pion results, $(\pi^+ + \pi^-)/2$, were used to extend neutral pion measurements at the lower limit of the p_T range from 1 to 0.2 GeV/c. To produce the average pion spectrum in $p + p$ [22] and $d + \mathrm{Au}$ collisions [24], we simultaneously fit $(\pi^+ + \pi^-)/2$ and π^0 spectra with the modified Hagedorn function [19]. Inclusion of the charged pion spectrum in the fit has a small effect in the 1–2 GeV/c overlap region, smaller than 5% compared to fitting neutral pions alone. The resulting fitted pion distributions are used to calculate ω/π ratios for $p + p$ and $d + \mathrm{Au}$. Uncertainties for the fit values are evaluated by taking into account statistical and systematic uncertainties of the experimental points as described in [7,25].

Figure 7 presents the ω/π ratio measured in $p + p$ collisions at $\sqrt{s} = 200$ GeV as a function of transverse momentum. Open markers show our previous measurements of the ω/π ratio [8]. One can see good agreement between previous results and this measurement. For completeness, we also present similar measurements performed in lower-energy

TABLE IV. The number of participating collisions ($\langle N_{\mathrm{part}} \rangle$) and the number of binary nucleon-nucleon collisions ($\langle N_{\mathrm{coll}} \rangle$).

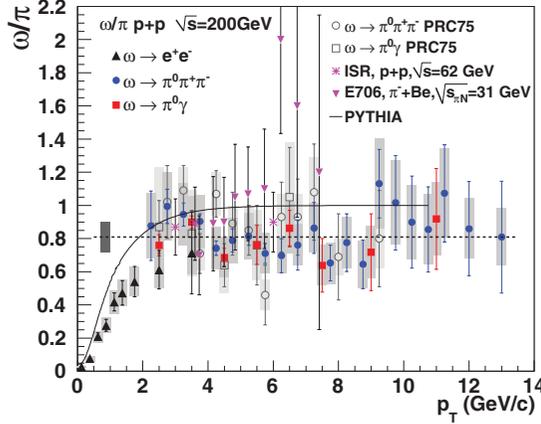| System	$\langle N_{\mathrm{part}} \rangle$	$\langle N_{\mathrm{coll}} \rangle$
$\mathrm{Au} + \mathrm{Au}$ MinBias	109.1 ± 4.1	257.8 ± 25.4
$\mathrm{Au} + \mathrm{Au}$ 0-20%	280.5 ± 4.6	783.2 ± 77.5
$\mathrm{Au} + \mathrm{Au}$ 20-60%	101.6 ± 5.4	197.5 ± 20.8
$\mathrm{Au} + \mathrm{Au}$ 60-92%	11.8 ± 2.1	11.5 ± 2.5
$\mathrm{Cu} + \mathrm{Cu}$ MinBias	34.6 ± 1.2	51.8 ± 5.6
$\mathrm{Cu} + \mathrm{Cu}$ 0-20%	85.9 ± 2.3	151.8 ± 17.1
$\mathrm{Cu} + \mathrm{Cu}$ 20-60%	33.2 ± 1.6	41.9 ± 4.8
$\mathrm{Cu} + \mathrm{Cu}$ 60-94%	6.5 ± 0.6	5.1 ± 0.7

FIG. 7. (Color online) Measured ω/π ratio as a function of p_T in $p + p$ collisions at $\sqrt{s} = 200$ GeV. (Dashed line) Fit of a constant value to data points at $p_T > 2$ GeV/c. The fit result is $0.81 \pm 0.02^{\text{stat}} \pm 0.09^{\text{syst}}$. (Gray box) The overall error of the fitting. (Solid line) The PYTHIA prediction [28] for $p + p$ at $\sqrt{s} = 200$ GeV. Shown for comparison are previously published results from PHENIX (PRC75) [8] and lower collision energies at $\sqrt{s_{\pi N}} = 31$ GeV (E706) [26] and $\sqrt{s} = 62$ GeV (ISR) [27].

experiments: $\pi + $Be at $\sqrt{s_{NN}} = 31$ GeV (E706 [26]), $p + p$ at $\sqrt{s} = 62$ GeV (ISR [27]). Please note that the branching ratio for the $\omega \to \pi^0 \gamma$ decay was set equal to $(8.8 \pm 0.5)\%$, which is 6% different from the latest PDG value of $(8.28 \pm 0.28)\%$.

Within measurement uncertainties, the ω/π ratio in hadronic interactions is energy independent at high p_T.

A linear fit to the ratio at $p_T > 2$ GeV/c gives a value of the linear coefficient consistent with zero within less then one standard deviation ($-0.013 \pm 0.009^{\text{stat}} \pm 0.014^{\text{syst}}$), indicating no significant p_T dependence of the ratio at $p_T > 2$ GeV/c. A fit to a constant gives a value of the ratio equal to $0.81 \pm 0.02^{\text{stat}} \pm 0.09^{\text{syst}}$ consistent with our previous measurement of $0.85 \pm 0.05^{\text{stat}} \pm 0.09^{\text{syst}}$ [8]. The PYTHIA prediction of the ω/π ratio, shown in Fig. 7 with a solid line, lies above the measured ratio.

The ω/π ratios measured in minimum bias $d + $Au, Cu + Cu, and Au + Au collisions at $\sqrt{s_{NN}} = 200$ GeV are presented in Fig. 8. As in the case of $p + p$ collisions, there is no indication that the ratios depend on transverse momentum for $p_T > 2$ GeV/c. Fits to a constant for $p_T > 2$ GeV/c give the following values of the ω/π ratio: $0.75 \pm 0.01^{\text{stat}} \pm 0.08^{\text{syst}}$ in $d + $Au, $0.71 \pm 0.07^{\text{stat}} \pm 0.07^{\text{syst}}$ in Cu + Cu, and $0.83 \pm 0.09^{\text{stat}} \pm 0.06^{\text{syst}}$ in MB Au + Au collisions. Within the uncertainties, the ω/π ratios measured in different collision systems for $p_T > 2$ GeV/c are in agreement. This agrees with previous measurements in $d + $Au [8] within the uncertainties. The ratios in various collision systems imply similar suppression factors and p_T dependencies within the uncertainties for the ω and π production in nucleus-nucleus collisions at high p_T.
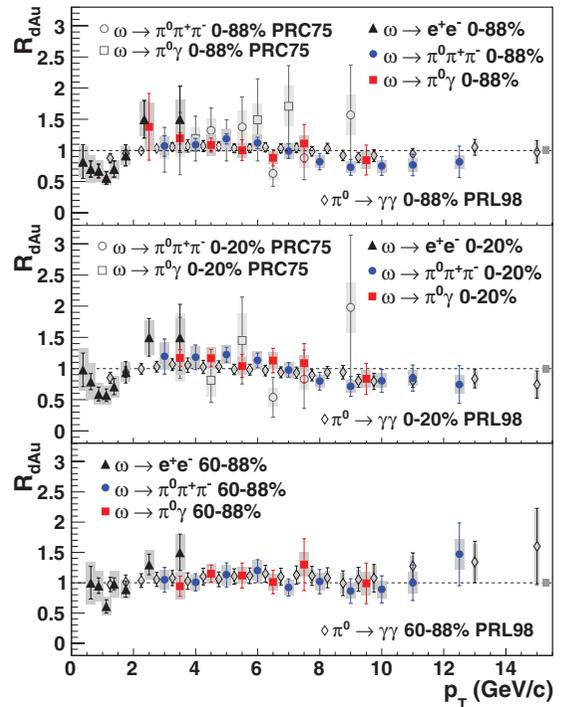

FIG. 8. (Color online) The ω/π ratios versus transverse momentum at $\sqrt{s_{NN}} = 200$ GeV in (a) $d + $Au collisions (0–88% centrality) for $\omega \to e^+ e^-$, $\pi^0 \pi^+ \pi^-$, and $\pi^0 \gamma$ and (b) Cu + Cu collisions (0–94% centrality) and Au + Au collisions (0–92% centrality) for $\omega \to \pi^0 \gamma$. The dashed lines and boxes are a fit of a constant value to the data points at $p_T > 2$ GeV/c in $p + p$ (Fit result: $0.81 \pm 0.02^{\text{stat}} \pm 0.09^{\text{syst}}$). The previously published data (PRC75) [8] are shown for comparison.

FIG. 9. (Color online) Nuclear modification factor, $R_{d\text{Au}}$, measured for the ω in 0–88, 0–20, and 60–88% centrality bins in $d + $Au collisions at $\sqrt{s} = 200$ GeV. The gray box at the rightmost end of the constant fit line shows the uncertainty of the fit. The previously published data for ω (PRC75) [8] and π^0 (PRL98) [24] are shown for comparison.

C. Nuclear modification factors

To quantify medium-induced effects on high p_T particle production, the nuclear modification factor is defined as

$$R_{AB}(p_T) = \frac{d^2 N_{AB}/dy\,dp_T}{\left(\langle N_{coll}\rangle/\sigma_{pp}^{inel}\right) \times d^2\sigma_{pp}/dy\,dp_T}, \qquad (3)$$

where $d^2 N_{AB}/dy\,dp_T$ is the differential yield per event in nucleus-nucleus collisions, $\langle N_{coll}\rangle$ is the number of binary nucleon-nucleon collisions averaged over the impact parameter range of the corresponding centrality bin calculated by Glauber Monte-Carlo simulation [14], and σ_{pp}^{inel} and $d^2\sigma_{pp}/dy\,dp_T$ are the total and differential cross sections for inelastic $p+p$ collisions, respectively. In the absence of medium-induced effects, the yield of high-p_T particles is expected to scale with $\langle N_{coll}\rangle$, resulting in $R_{AB} = 1$ at high-p_T.

Figure 9 presents R_{dAu} measured for the ω in minimum bias, most central and peripheral $d+$Au collisions at $\sqrt{s_{NN}} = 200$ GeV. Good agreement is observed between different decay modes and between new and previously published PHENIX ω results [8] shown with open markers. For comparison we also present π^0 results published in Ref. [24]. In peripheral collisions, the measured values of R_{dAu} are consistent with unity over the whole p_T range of measurements. In most central collisions, a modest Cronin-like enhancement is observed in a range of p_T from 2 to 6 GeV/c and suppression of ω production at $p_T > 8$ GeV/c. A similar enhancement at 2–6 GeV/c was previously observed for neutral and charged pions [22,24] and ϕ mesons [29]. Suppression of ω production at higher p_T is in agreement with π^0 results [24]. Similarity of

FIG. 11. (Color online) R_{AA} for the ω meson integrated over the range $p_T > 7$ GeV/c as a function of the number participating nucleons (N_{part}). Results for π^0 (PRL101) [4] and η (PRC82) [5] are shown for comparison. The dashed line shows the fitted fractional energy loss function, $R_{AA} = (1 - S_0 N_{part}^a)^{n-2}$.

the observed effects for the mesons with very different masses suggests that the collective nuclear effects occur at the partonic level [30–32].

Figure 10 shows the nuclear modification factors measured in Cu+Cu and Au+Au collisions at $\sqrt{s_{NN}} = 200$ GeV as a function of p_T. Results are presented for minimum bias, most central (0–20%), midcentral (20–60%) and peripheral (60–94% in Cu+Cu; 60–92% in Au+Au) collisions. The nuclear modification factors do not depend on p_T for $p_T > 6$ GeV/c at all centralities. For $N_{part} > 34$ suppression of ω production begins to be observed, with suppression increasing as N_{part} increases.

Figure 11 shows R_{AA} values integrated for $p_T > 7$ GeV/c as a function the number of participants. For ω mesons we present four centrality bins in $d+$Au, and three centrality bins in Cu+Cu and Au+Au. For comparison the average values of R_{AA} for π^0 [4] and η mesons [5] mesons for $p_T > 7$ GeV/c are also plotted. To see whether the ω follows the suppression pattern of π^0 and η, the integrated R_{AA} vs N_{part} dependence is fit to a fractional energy loss function $R_{AA} = (1 - S_0 N_{part}^a)^{n-2}$ [4,33]. The parameter n, which is an exponent of the power law fit to the ω p_T spectrum measured in $p+p$ for $p_T > 5$ GeV/c [7], was fixed to 8. The fitting gives χ^2/ndf less than three and parameters $S_0 = (9.9 \pm 0.7) \times 10^{-3}$ and $a = 0.55 \pm 0.01$. As in Ref. [4], we find the parameter a consistent with predictions of the GLV [34] and PQM [6] models ($a \sim 2/3$). Therefore, we can conclude that ω production has a similar suppression pattern as π^0 and η, which supports the scenario that the energy loss takes place at the parton level in the hot and dense medium formed in the collisions.

V. SUMMARY

We measured production of the ω meson via both leptonic and hadronic decay channels in $p+p$, $d+$Au, Cu+Cu, and Au+Au at $\sqrt{s_{NN}} = 200$ GeV. The invariant transverse momentum spectra show good agreement in different decay channels in $p+p$ and $d+$Au. The R_{dAu} shows a moderate Cronin-like enhancement at intermediate p_T 2–6 GeV/c

FIG. 10. R_{AA} of the ω in Cu+Cu and Au+Au collisions from the $\omega \to \pi^0\gamma$ decay channel for three centrality bins and minimum bias. The uncertainty in the determinations of $p+p$ scaling are indicated in gray boxes near the rightmost end of the $R_{AA} = 1$ dashed lines. Rhombuses in each plot are R_{AA} of π^0 in Cu+Cu [23] and Au+Au [4] shown as a comparison.
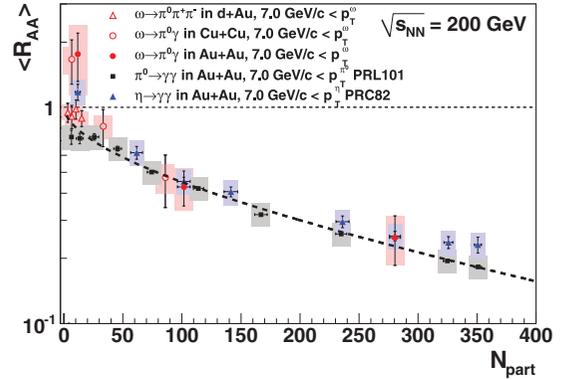
and suppression for $p_T > 8$ GeV/c in most central $d + $ Au collisions. The measurement of the nuclear modification factor for the ω meson in Cu $+$ Cu and Au $+$ Au collisions show that ω production has a similar suppression pattern as the π^0 and η within model agreement, thus supporting the scenario that the energy loss takes place at the partonic level in the hot and dense medium formed in the collisions.

[1] X. N. Wang, Phys. Lett. B **579**, 299 (2004).

[2] S. Adler *et al.* (PHENIX Collaboration), Phys. Rev. Lett. **96**, 202301 (2006).

[3] B. Abelev *et al.* (STAR Collaboration), Phys. Rev. C **80**, 44905 (2009).

[4] A. Adare *et al.* (PHENIX Collaboration), Phys. Rev. Lett. **101**, 232301 (2008).

[5] A. Adare *et al.* (PHENIX Collaboration), Phys. Rev. C **82**, 011902 (2010).

[6] C. Loizides (PQM Collaboration), Eur. Phys. J. C **49**, 339 (2007).

[7] A. Adare *et al.* (PHENIX Collaboration), Phys. Rev. D **83**, 052004 (2011).

[8] S. Adler *et al.* (PHENIX Collaboration), Phys. Rev. C **75**, 051902 (2007).

[9] K. Nakamura *et al.* (Particle Data Group Collaboration), J. Phys. G **37**, 075021 (2010).

[10] S. Adler *et al.* (PHENIX Collaboration), Phys. Rev. C **75**, 024909 (2007).

[11] K. Adcox *et al.* (PHENIX Collaboration), Nucl. Instrum. Methods A **499**, 469 (2003).

[12] K. Adcox *et al.* (PHENIX Collaboration), Nucl. Instrum. Methods A **499**, 469 (2003).

[13] M. Allen *et al.* (PHENIX Collaboration), Nucl. Instrum. Methods A **499**, 549 (2003).

[14] R. J. Glauber and G. Matthiae, Nucl. Phys. B **21**, 135 (1970).

[15] M. L. Miller, K. Reygers, S. J. Sanders, and P. Steinberg, Annu. Rev. Nucl. Part. Sci. **57**, 205 (2007).

[16] M. Aizawa *et al.* (PHENIX Collaboration), Nucl. Instrum. Methods A **499**, 508 (2003).

[17] K. Adcox *et al.* (PHENIX Collaboration), Nucl. Instrum. Methods A **499**, 489 (2003).

[18] L. Aphecetche *et al.* (PHENIX Collaboration), Nucl. Instrum. Methods A **499**, 521 (2003).

[19] A. Adare *et al.* (PHENIX Collaboration), Phys. Rev. C **81**, 034911 (2010).

[20] C. Tsallis, J. Stat. Phys. **52**, 479 (1988).

[21] S. Adler *et al.* (PHENIX Collaboration), Phys. Rev. Lett. **95**, 202001 (2005).

[22] S. S. Adler *et al.* (PHENIX Collaboration), Phys. Rev. C **74**, 024904 (2006).

[23] A. Adare *et al.* (PHENIX Collaboration), Phys. Rev. Lett. **101**, 162301 (2008).

[24] S. S. Adler *et al.* (PHENIX Collaboration), Phys. Rev. Lett. **98**, 172302 (2007).

[25] A. Adare *et al.* (PHENIX Collaboration), Phys. Rev. C **77**, 064907 (2008).

[26] L. Apanasevich *et al.* (E706 Collaboration), arXiv:hep-ex/0004012 (2000).

[27] M. Diakonou *et al.* (ISR Collaboration), Phys. Lett. B **89**, 432 (1980).

[28] T. Sjostand, L. Lonnblad, and S. Mrenna arXiv:hep-ph/0108264 (2001).

[29] A. Adare *et al.* (PHENIX Collaboration), Phys. Rev. C **83**, 024909 (2011).

[30] R. J. Fries, B. Muller, C. Nonaka, and S. A. Bass, Phys. Rev. C **68**, 044902 (2003).

[31] R. C. Hwa and C. B. Yang, Phys. Rev. C **70**, 024905 (2004).

[32] J. W. Cronin *et al.*, Phys. Rev. D **11**, 3105 (1975).

[33] K. Adcox *et al.* (PHENIX Collaboration), Nucl. Phys. A **757**, 184 (2005).

[34] M. Gyulassy, P. Levai, and I. Vitev (GLV Collaboration), Phys. Rev. Lett. **85**, 5535 (2000).